Article

Effect of TiO$_2$ Additives on the Stabilization of *h*-YbFeO$_3$ and Promotion of Photo-Fenton Activity of *o*-YbFeO$_3$/*h*-YbFeO$_3$/*r*-TiO$_2$ Nanocomposites

Sofia Tikhanova [1,2,*] , Anna Seroglazova [1,2], Maria Chebanenko [1], Vladimir Nevedomskiy [1] and Vadim Popkov [1]

1   Ioffe Institute, 194021 Saint Petersburg, Russia
2   Saint-Petersburg State Institute of Technology, 190013 Saint Petersburg, Russia
*   Correspondence: tihanova.sof@gmail.com

Abstract: Nanostructured hexagonal rare-earth orthoferrites (*h*-RfeO$_3$, R = Sc, Y, Tb-Lu) are well known as a highly effective base for visible-light-driven heterojunction photocatalysts. However, their application is limited by metastability, leading to difficulties in synthesis due to the irreversible transformation to a stable orthorhombic structure. In this work, we report on a simple route to the stabilization of *h*-YbFeO$_3$ nanocrystals by the synthesis of multiphase nanocomposites with titania additives. The new I-type heterojunction nanocomposites of *o*-YbFeO$_3$/*h*-YbFeO$_3$/*r*-TiO$_2$ were obtained by the glycine–nitrate solution combustion method with subsequent heat treatment of the products. An increase in the mole fraction of the *h*-YbFeO$_3$ phase in nanocomposites was found with the titanium addition, indicating its stabilizing effect via limiting mass transfer over heat treatment. The complex physicochemical analysis shows multiple contacts of individual nanocrystals of *o*-YbFeO$_3$ (44.4–50.6 nm), *h*-YbFeO$_3$ (7.5–17.6 nm), and rutile *r*-TiO$_2$ (~5 nm), confirming the presence of the heterojunction structure in the obtained nanocomposite. The photocatalytic activity of *h*-YbFeO$_3$/*o*-YbFeO$_3$/*r*-TiO$_2$ nanocomposites was evaluated by the photo-Fenton degradation of the methyl violet under visible light ($\lambda \geq 400$ nm). It was demonstrated that the addition of 5 mol.% of TiO$_2$ stabilizes *h*-YbFeO$_3$, which allowed us to achieve a 41.5 mol% fraction, followed by a three-time increase in the photodecomposition rate constant up to 0.0160 min^{-1}.

Keywords: ytterbium orthoferrite; titanium dioxide; solution combustion synthesis; heterojunctions; photocatalysts; Fenton-like processes

1. Introduction

Metal oxide nanoparticles have been well-described in a number of applications involving biomedicine and industry [1–3]. As a perspective class of oxide-based materials, orthoferrites of rare earth elements have gained considerable interest among researchers due to their structural [4–8], magnetic [6,9–11], electrical [6,12], and photocatalytic [13–18] properties. This class of compounds has found practical applications as a material for catalysts [19], magnetic resonance imaging [20,21], bio-medical drug delivery [22,23], sensors [24,25], and pigments [26,27]. Notably, ytterbium orthoferrite can be used as a highly efficient photocatalyst whose activity depends on its crystal structure [28]. YbFeO$_3$ is characterized by an orthorhombic perovskite structure (*Pbnm/Pnma*), which is thermodynamically stable [29]. However, a hexagonal phase was also obtained, first in thin films and then in bulk form. Depending on the synthesis conditions, the hexagonal phase can be either polar P6$_3$cm or nonpolar P6$_3$/mmc [30]. It is known that substances in the metastable states often exhibit unique properties, for example, higher specific surface area [31] and narrower distribution of crystallite sizes [13].

On the one hand, it has been reported that the hexagonal form (*h*-YbFeO$_3$) demonstrates higher photocatalytic activity than that of *o*-YbFeO$_3$ under the same conditions [28].

On the other hand, *h*-YbFeO$_3$ shows high instability and a tendency to transform easily in the stable *o*-YbFeO$_3$ phase [32,33].

Previously, several ways of stabilization by creating spatial constraints were found. Some of the most common are self-organized [34,35] and template-assisted combustion processes [36]. However, the stabilization effect of the second phase addition has never been reported. Recently, we confirmed the possibility of the stabilization of *h*-YbFeO$_3$ by the CeO$_2$ extra phase [32]. In the present work, for the first time, the possibility of creating additional spatial restrictions due to the insertion of the second TiO$_2$ phase was demonstrated and the synthesis of novel I-type heterojunction nanocomposites of *o*-YbFeO$_3$/*h*-YbFeO$_3$/*r*-TiO$_2$ was performed.

In this work, TiO$_2$ was used as an extra phase because of its high photocatalytic activity as a co-catalyst in the photo-Fenton-like degradation processes [37]. Additionally, titania dioxide is a highly stable and environmentally safe photocatalyst in the near-UV or even visible light (due to dye-driven photo-sensibilization) regions [38,39]. To promote the uniform distribution of the compounds, the solution combustion method was used and successfully executed.

2. Materials and Methods

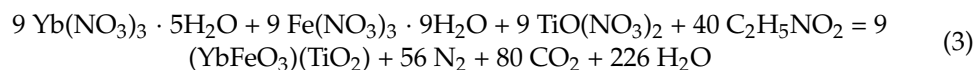### 2.1. Synthesis of YbFeO$_3$-Based Photocatalysts

2.1.1. Synthesis of the Titanyl Nitrate TiO(NO$_3$)$_2$ Solution

The synthesis of *h*-YbFeO$_3$/*o*-YbFeO$_3$/TiO$_2$ nanocomposites included the preparation of titanyl nitrate from titanium tetrachloride TiCl$_4$. Firstly, distilled water was added to 1 mL of TiCl$_4$ with constant stirring to form a clear solution of TiCl$_4$. Then, 2 mL of 5% solution of NH$_4$OH was added to obtain a white precipitate of TiO(OH)$_2$. Finally, it was completely dissolved in concentrated HNO$_3$. The process can be described by the following reactions:

$$TiCl_4 + 3 NH_4OH = TiO(OH)_2 + 3 NH_3 + 4 HCl \tag{1}$$

$$TiO(OH)_2 + 2 HNO_3 = TiO(NO_3)_2 + 2 H_2O \tag{2}$$
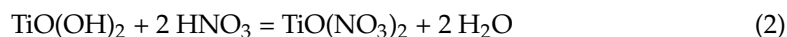
2.1.2. Synthesis of o-YbFeO$_3$/h-YbFeO$_3$/TiO$_2$ Nanocomposites

Series of *h*-YbFeO$_3$/*o*-YbFeO$_3$/TiO$_2$ samples with a molar fraction of titanium dioxide of 0, 2.5, 5, 7.5 mol.% were obtained by glycine–nitrate solution combustion method followed by subsequent heat treatment of the products. The precursor salts Yb(NO$_3$)$_3$·6H$_2$O (99.5%) 0.5469 g, Fe(NO$_3$)$_3$·9H$_2$O (98.0%) 0.5149 g, and glycine (C$_2$H$_5$NO$_2$, 98.5%) 0.1168 g were solved in 10 mL of distilled water with 0.1, 0.2, 0.3, and 0.4 mL of titanyl nitrate TiO(NO$_3$)$_2$ solution (Section 2.1.1) for the 2.5, 5, and 7.5 samples, respectively. The considered combustion process is described by the following reaction scheme:

$$9 Yb(NO_3)_3 \cdot 5H_2O + 9 Fe(NO_3)_3 \cdot 9H_2O + 9 TiO(NO_3)_2 + 40 C_2H_5NO_2 = 9 (YbFeO_3)(TiO_2) + 56 N_2 + 80 CO_2 + 226 H_2O \tag{3}$$

To achieve the complete dissolution of components, the reaction solution was mixed for 15 min at room temperature. After that, the reaction mixture was heated in a sand bath until the water evaporated and the solution self-ignited. As a final product of combustion, the foam-like porous substance was pounded in a mortar to form a powder. Then it was calcinated at 800 °C for 24 h to achieve the complete removal of organic residues and form crystalline products. The ratio of the contents of glycine and nitrate ions (glycine to nitrate ratio or *G/N*) in the reaction solution equaled 0.2. In the excess of oxidizer, the glowing mode of combustion is applied, and the formation of X-ray amorphous products is promoted.

2.2. Characterization

The elemental composition was investigated by energy-dispersive X-ray spectroscopy (EDXS, Tescan Vega 3 SBH, Oxford INCA X-act, TESCAN Brno s.r.o., Brno, Czechia). The crystal structure was investigated by X-ray diffraction (XRD, Rigaku SmartLab 3, Rigaku

Corporation, Tokyo, Japan) using Cu Kα radiation (λ = 1.540598 Å). The average crystallite size was calculated from the broadening of X-ray diffraction lines using the method of fundamental parameters implemented in the SmartLab Studio II software package (Rigaku Corporation, Tokyo, Japan). Quantitative X-ray phase analysis was conducted by means of the Rietveld method. The morphology and microstructure were investigated by scanning electron microscopy (SEM, Tescan Vega 3 SBH, TESCAN Brno s.r.o., Brno, Czechia)) and transmission electron microscopy (TEM, ZEISS Ultra 55 microscope, FELMI ZFE, Oberkochen, Germany) in the image and selected area electron diffraction (SAED) mode. The diffuse reflectance spectra in the UV–visible region (DRS, Avaspec-ULS2048, AvaSphere-30-Refl, Avantes, Apeldoorn, The Netherlands) were recorded at room temperature in the range of 400–750 nm using an AvaSphere-30-Refl integrating sphere. The specific surface of the samples, pore volume, and pore size distribution were determined by adsorption-structural analysis (ASA, Micromeritics ASAP 2020, Norcross, GA, USA). Sorption–desorption isotherms were obtained at a liquid nitrogen temperature of 77 K.

2.3. Photocatalytic Experiments

The photo-Fenton-like degradation of methyl violet (MV) with the addition of hydrogen peroxide was used to investigate the photocatalytic activity of the produced catalysts. The photocatalytic experiment was carried out under visible light irrigation λ_{max} = 410 nm. The typical process was described in detail in previous work [16]. To establish the adsorption equilibrium, the reaction solutions were stirred in darkness for 30 min before the start of the photocatalytic experiment. For the absorption spectra measurements and the concentration of the MV determination, AvaLight-XE light source and AvaSpec-ULS2048 spectrometer were used. Decolorization of the dye was measured every 10 min.

3. Results and Discussion

3.1. SEM, EDXS, and Elemental Mapping

The energy-dispersive X-ray spectroscopy (EDXS) results (Figure 1) demonstrate that, for all samples, the Yb: Fe ratio is approximately equal to 1. In the samples containing titanium dioxide, its amount corresponds to the values declared during the synthesis. Thus, the planned ratios of key elements are achieved within the error of the determination.
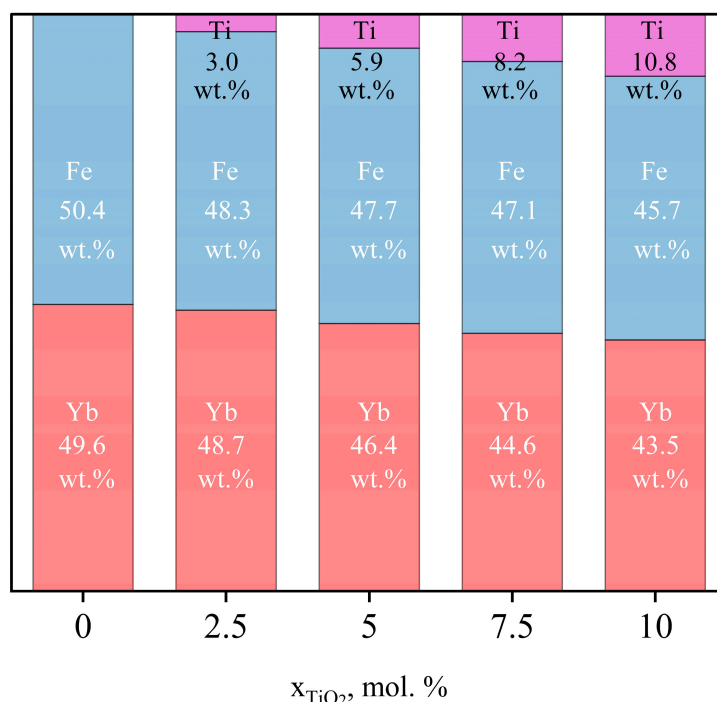

Figure 1. The elemental composition of samples concerning the main elements (in wt.%).

Energy dispersive elemental mapping of a sample containing 5 mol.% of TiO$_2$ Figure 2c shows that the key elements are distributed uniformly. Single-element mapping Figure 2d,f confirms the absence of accumulation zones of individual chemical elements in the sample. Microphotography of the area used for mapping Figure 2a,b reflects the foam-like morphology typical for samples synthesized by the solution combustion method [40–42].
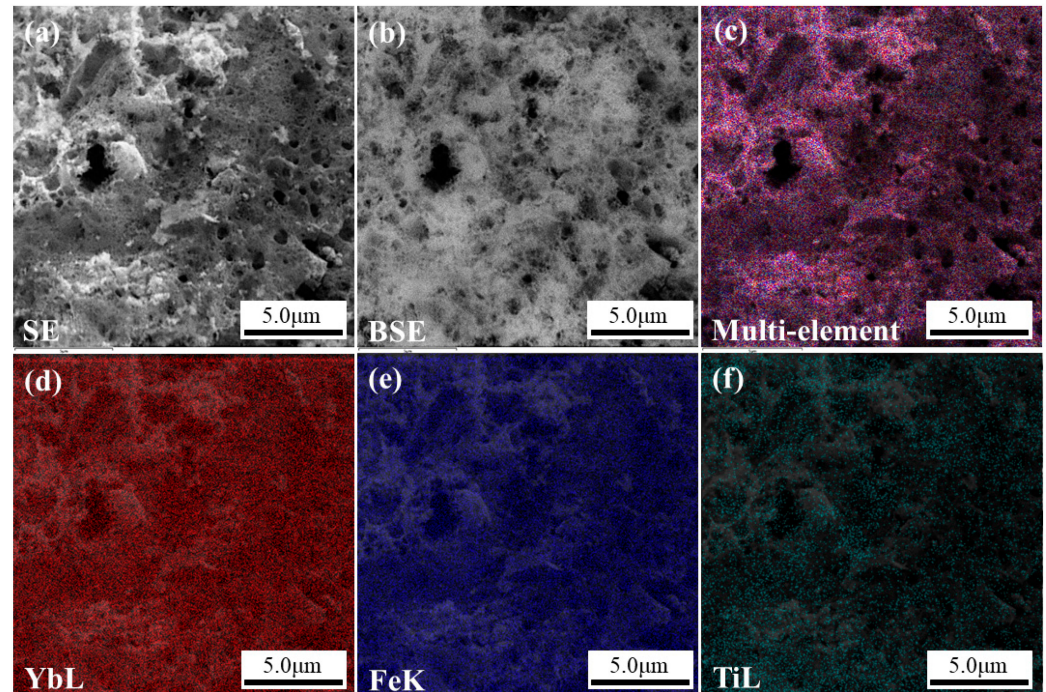

Figure 2. SEM images obtained on SE (**a**) and BSE (**b**) detectors and EDXS multi-element (**c**) and single element (**d**–Yb, **e**–Fe, **f**–Ti) mapping of a sample containing 5 mol.% of TiO$_2$.

3.2. PXRD

Figure 3a demonstrates the PXRD patterns measured at room temperature with ground samples after heat-treatment at 800 °C. All peaks of YbFeO$_3$ can be well-indexed to the characteristic XRD peaks of the orthorhombic structure according to the ICSD card No. 189735. The absence of any additional peaks indicates the successful synthesis of pure o-YbFeO$_3$ by the solution combustion method. For all the samples synthesized with the addition of TiO$_2$, the presence of h-YbFeO$_3$ is observed. For samples containing from 2.5 to 7.5 mol.% of TiO$_2$, only o-YbFeO$_3$, h-YbFeO$_3$, and r-TiO$_2$ phases can be indicated. There were no other peaks related to impurities for these samples. A further increase in the mole fraction of titanium dioxide leads to the formation of a mixture of phases o-YbFeO$_3$, h-YbFeO$_3$, Yb$_2$Ti$_2$O$_7$, and Fe$_2$O$_3$.

Crystallite sizes for the major phases Figure 3b varied in the range of 44.4–50.6 nm for o-YbFeO$_3$ and 7.5–17.6 nm for h-YbFeO$_3$, which is in consonance with existing research. The minimum size of a h-YbFeO$_3$ crystallite is observed for the sample containing 5 mol.% of TiO$_2$. The determination of crystallite sizes for the minor phases is complicated due to the overlaying of the peaks.

The degree of conversion dependences in Figure 3c were evaluated by the Rietveld refinement method. Structural parameters and criteria of fit of the typical refinement for the sample containing 5 mol.% of TiO$_2$ are presented in Figure 4. The refinement data confirms that the o-YbFeO$_3$/h-YbFeO$_3$/r-TiO$_2$–5% sample consist of three phases: o-YbFeO$_3$ with orthorhombic structure, space group *Pbnm*; h-YbFeO$_3$ with hexagonal structure, space group *P63/mmc*; r-TiO$_2$ with rutile structure, and space group *P 42/m n m*. The investigated unit cell parameters are in good agreement with literature data. The value of R$_{wp}$, R$_p$, and R$_e$ parameters show that the refinements were correct.
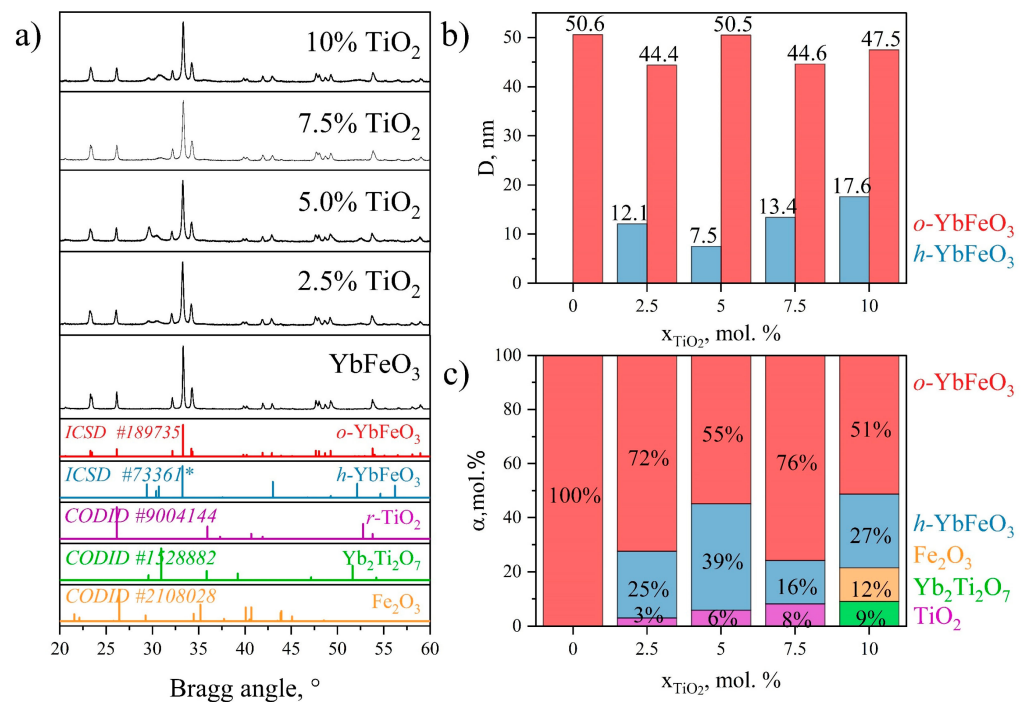
Figure 3. PXRD patterns of o-YbFeO$_3$/h-YbFeO$_3$/r-TiO$_2$ (**a**), average crystallite sizes (D, nm) (**b**) and molar fraction (α, mol.%) (**c**) versus TiO$_2$ content (mol.%).

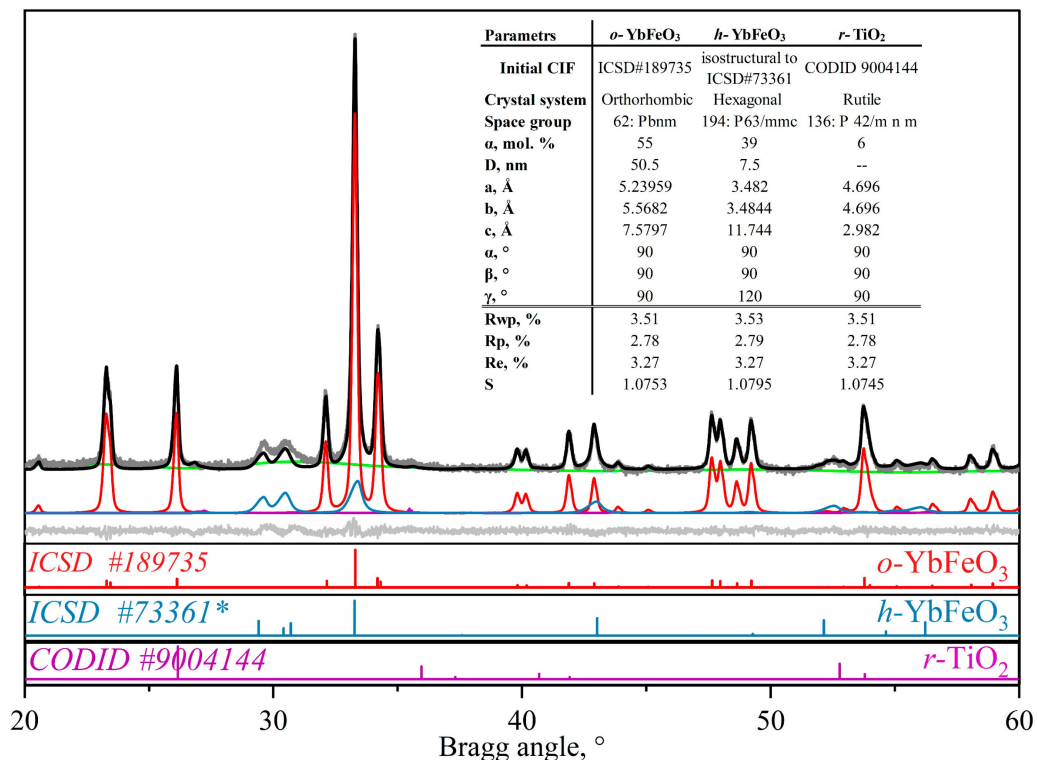| Parametrs	o-YbFeO$_3$	h-YbFeO$_3$	r-TiO$_2$
Initial CIF	ICSD#189735	isostructural to ICSD#73361	CODID 9004144
Crystal system	Orthorhombic	Hexagonal	Rutile
Space group	62: Pbnm	194: P63/mmc	136: P 42/m n m
α, mol. %	55	39	6
D, nm	50.5	7.5	--
a, Å	5.23959	3.482	4.696
b, Å	5.5682	3.4844	4.696
c, Å	7.5797	11.744	2.982
α, °	90	90	90
β, °	90	90	90
γ, °	90	120	90
Rwp, %	3.51	3.53	3.51
Rp, %	2.78	2.79	2.78
Re, %	3.27	3.27	3.27
S	1.0753	1.0795	1.0745

Figure 4. Rietveld refinement results for the X-ray diffraction of o-YbFeO$_3$/h-YbFeO$_3$/r-TiO$_2$- 5%.

According to PXRD data, the dependences of the degree of conversion of the main crystalline phases on the proportion of added titanium dioxide were calculated Figure 3c. As the content of titanium dioxide in the composite increases, the mole fraction of TiO$_2$ increases linearly, which is consistent with the EDX data. In addition, when titanium dioxide is added, the formation of the h-YbFeO$_3$ is observed. The maximum molar fraction

of h-YbFeO$_3$ phase is 39 mol.% for the sample with 5 mol.% of TiO$_2$. For the sample containing 10 mol.% of TiO$_2$ the molar fraction of phase containing titanium agrees with the increase in the added amount of titanyl nitrate.

3.3. HR-TEM and SAED

The morphology and microstructure of the *h*-YbFeO$_3$/*o*-YbFeO$_3$/TiO$_2$–5% sample were investigated by transmission electron microscopy (TEM) Figure 5. The TEM image of the nanocomposite presents the shaped crystals surrounded by a foam-like substance. As was determined by XRD, the crystalline size for *o*-YbFeO$_3$ is approximately 50 nm, which means that we can assume that the shaped crystals are associated with *o*-YbFeO$_3$, whose morphology is typical for heat-treated glycine-nitrate combustion products. The foam-like structure is more usual for products without heat treatment and for incompletely formed particles [28].
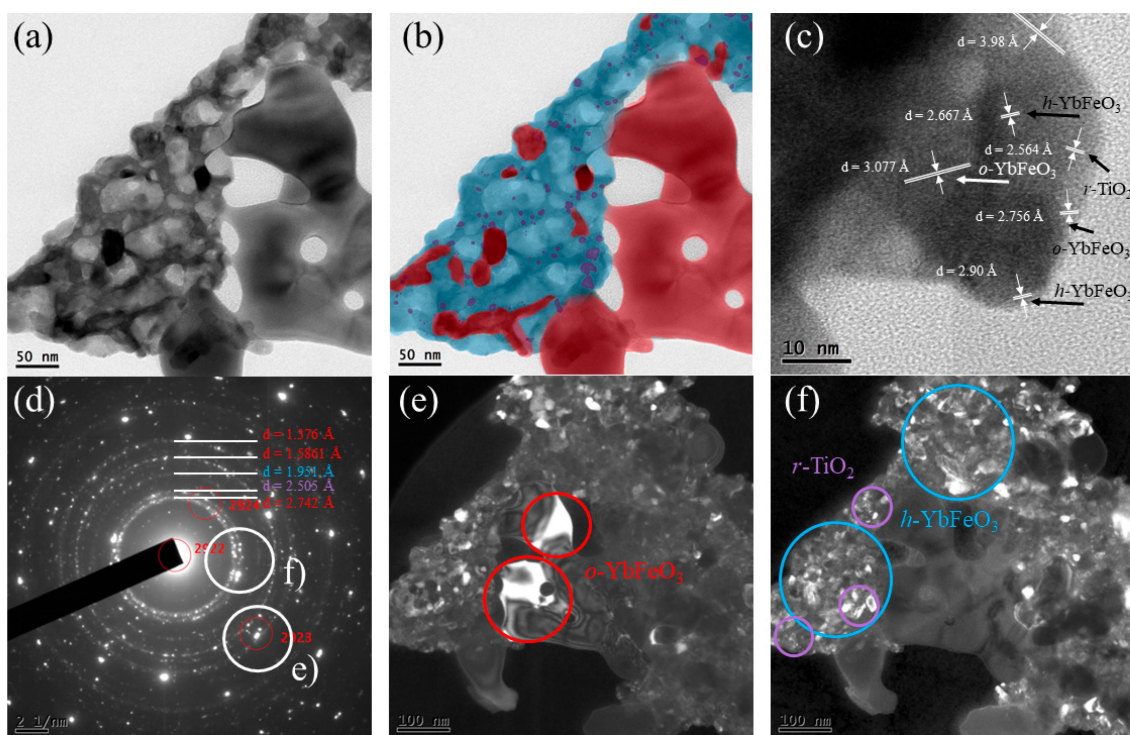

Figure 5. TEM images of the *h*-YbFeO$_3$/*o*-YbFeO$_3$/TiO$_2$–5% sample: (**a**) an overview of the *o*-YbFeO$_3$/*h*-YbFeO$_3$/TiO$_2$ nanocomposite, (**b**) color designation of phases: red—*o*-YbFeO$_3$, blue—*h*-YbFeO$_3$, purple—*r*-TiO$_2$, (**c**) the *h*-YbFeO$_3$ to *o*-YbFeO$_3$ and to *r*-TiO$_2$ heterojunction, (**d**) selected area transmission electron diffraction (SAED) pattern and dark-field TEM of *o*-YbFeO$_3$ (**e**) and *h*-YbFeO$_3$, *r*-TiO$_2$ (**f**) nanocrystals.

Therefore, the SAED pattern Figure 5d from Figure 5a confirms the absence of an amorphous phase. The dark-field TEM of single peaks Figure 5e, which are typical for monocrystals, confirms that the shaped crystals are *o*-YbFeO$_3$. The smaller light areas in the foam-like zone show the mixture of phases in it. The dark-field TEM of multiple ring peaks Figure 5f, which are typical for polycrystals, show the presence of small crystals in interporous substances.

For clearer phase determination, d-spacing was calculated from the SAED pattern. According to the results presented in Table 1, rings 1, 4, 5 are associated with *o*-YbFeO$_3$; the 2 is *r*-TiO$_2$, and the 3 is *h*-YbFeO$_3$. The crystallite size of *r*-TiO$_2$ is about 5 nm due to TEM results. The colored scheme of relative phase distribution shows the individual phases are in multiple contacts, which confirms the formation of the nanocomposite with a heterojunction structure.

Table 1. Results of phase analysis by SAED.

Ring №	D-Spacing, Å	Ref. d-Spacing, Å	Hkl	Phase
1	2.742	2.780	0 2 0	o-YbFeO$_3$
2	2.471	2.505	1 0 1	r-TiO$_2$
3	1.950	1.951	0 0 6	h-YbFeO$_3$
4	1.605	1.586	1 3 2	o-YbFeO$_3$
5	1.373	1.376	3 2 2	o-YbFeO$_3$

The formation of heterojunction was additionally confirmed by HR-TEM Figure 5c. The *d*-spacing was calculated from the HR-TEM image for the phase determination. As shown, the o-YbFeO$_3$ crystal is surrounded by r-TiO$_2$ and h-YbFeO$_3$ crystals.

As was previously reported, the presence of an inert phase prevents mass transfer and interrupts the structural transition hexagonal → orthorhombic ytterbium orthoferrite [32]. It can be surmised that the formation of o-YbFeO$_3$ was interrupted by r-TiO$_2$ particles on the board between shaped and foam-like areas. The mass transfer from h-YbFeO$_3$ to o-YbFeO$_3$ becomes difficult and the formation of h-YbFeO$_3$ crystals takes place. Consequently, we can assume that TiO$_2$ has a stabilizing effect on h-YbFeO$_3$.

3.4. Low-Temperature N$_2$ Sorption–Desorption

For a more detailed study of the specific surface area, average pore size, and volume of the obtained nanopowders, an adsorption structural analysis was performed using a low-temperature adsorption–desorption of nitrogen (77 K). Figure 6 presents the results of the experiment. As can be noticed from Figure 6a, the N$_2$ adsorption–desorption isotherm obtained for YbFeO$_3$ presented the type II isotherm with H3 hysteresis loop, and the classical type IV isotherm with H4 hysteresis loop was obtained for other samples containing TiO$_2$. The change in the isotherm type and the form of the loop results from the appearance of h-YbFeO$_3$ in the samples [28].
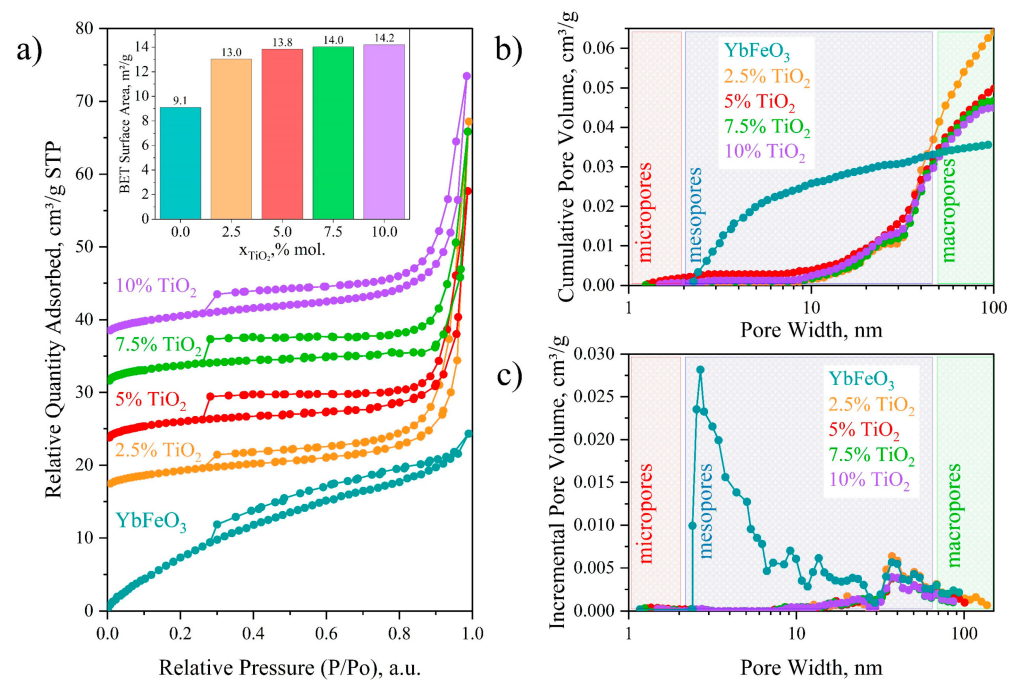

Figure 6. Low-temperature N$_2$ sorption–desorption isotherms (**a**), cumulative (**b**), and incremental (**c**) pore volume distribution of h-YbFeO$_3$/o-YbFeO$_3$/TiO$_2$ nanocomposites.

The surface area of the o-YbFeO$_3$/h-YbFeO$_3$/TiO$_2$ samples calculated by the BET method is presented as an inset in Figure 6a. According to the obtained data, the addition of up to 2.5 mol.% of titanium dioxide promotes an increase in the specific surface area

from 9.1 to 13.0 m^2/g. However, with further increase in the proportion of TiO$_2$, a smoother asymptotic increase is observed, and for samples containing 5–10 mol.% of titanium dioxide, the value of the specific surface remains practically unchanged. The pure YbFeO$_3$ sample presents a mesoporous structure, whereas other samples have a macroporous structure. The absence of micropores explains the relatively low surface area. Because of their small size, the *h*-YbFeO$_3$ and TiO$_2$ nanoparticles can fill the mesopores in the *o*-YbFeO$_3$ matrix and decrease the average surface.

3.5. DRS

The optical absorption property of h-YbFeO$_3$/o-YbFeO$_3$/TiO$_2$ was analyzed via UV-vis diffuse reflectance spectroscopy, and the results are shown in Figure 7a. The UV–visible absorption spectra of the synthesized nanocomposites were recorded in the range of wavelength of 400–750 nm. The light reflection spectra exhibit the reflection bands in the visible region, implying that those samples should be effective as visible light photocatalysts. Samples with 2.5 and 5 mol.% of TiO$_2$ show the most intensive absorption in the visible light region, which makes them perspective for visible-light-driven photocatalytic processes.
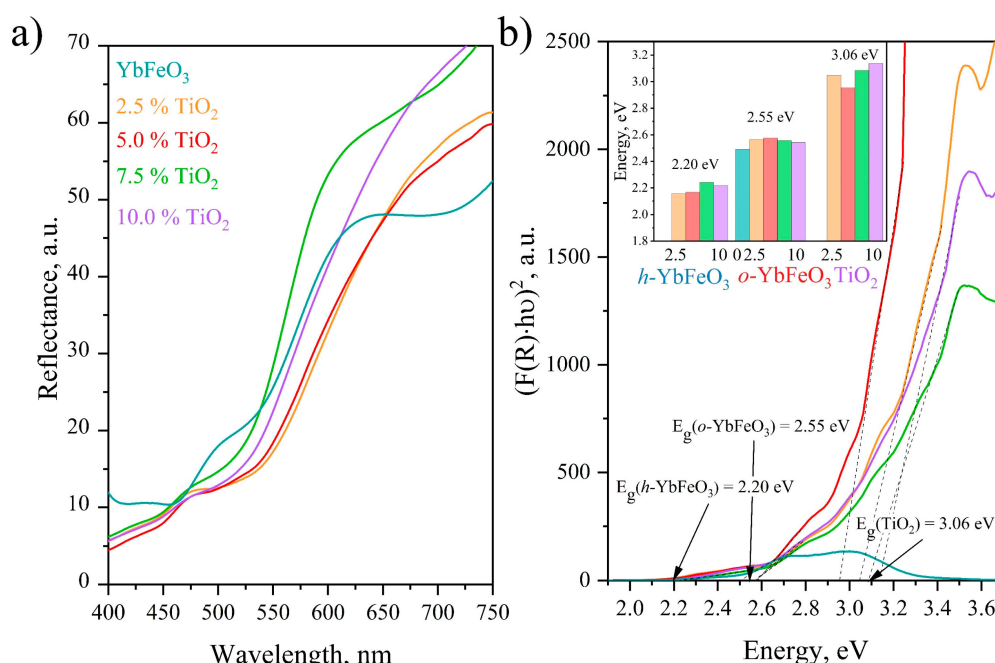

Figure 7. Diffuse reflectance spectra (**a**), Tauc plots (**b**), and band gap energy values (inset in b) of the *o*-YbFeO$_3$/*h*-YbFeO$_3$/TiO$_2$ samples.

The obtained samples demonstrate active absorption in the visible region of the spectrum, and the inflections in the reflection curves indicate the multiphase nature of the samples. The Tauc plot obtained by analyzing the reflectance measurement with Kubelka–Munk (KM) emission function to determine the band gaps of these phases Figure 7b, and the calculation results are presented in the inset. Considering that the calculated band gap values (E$_g$) for each of the phases change unsystematically, it can be assumed that they do not depend on the proportion of added titanium dioxide. The average E$_g$ values were 2.55 eV × (*o*-YbFeO$_3$), 2.20 eV (*h*-YbFeO$_3$), and 3.06 eV (TiO$_2$), which corresponds with the existing research [43,44]. According to the literature data, the band gap value of 3.1 eV is associated with the rutile TiO$_2$ [45]. It can be established that the resulting composite is based on individual phases of *o*-YbFeO$_3$, *h*-YbFeO$_3$, and *r*-TiO$_2$.

As a result of calculations presented in Table 2, the electronic structure parameters of *o*-YbFeO$_3$/*h*-YbFeO$_3$/TiO$_2$ nanocomposite were determined [28,46]. The relative position of the valence and conduction bands confirms the formation of a type I heterojunction

structure, which leads to the suppression of recombination of electron–hole pairs in photo-Fenton-like processes.

Table 2. Parameters of the electronic structure of o-YbFeO$_3$/h-YbFeO$_3$/TiO$_2$ nanocomposite.

	E_g, эВ	χ, эВ;	E_{VB}, эВ	E_{CB}, эВ
h- YbFeO$_3$	2.2	5.57	2.17	−0.03
o- YbFeO$_3$	2.55	5.57	2.35	−0.20
TiO$_2$	3.06	5.81	2.84	−0.22

3.6. Photo-Fenton-like Photocatalytic Activity

The photocatalytic activity of o-YbFeO$_3$/h-YbFeO$_3$/TiO$_2$ nanocomposites was evaluated by the photodegradation of the typical organic dye methyl violet (MV) under visible light irrigation, and the time-dependent photodegradation of MV is illustrated in Figure 8a. The high rate of discoloration of the solution shows that the resulting nanocomposites are effective catalysts for Fenton processes [46].
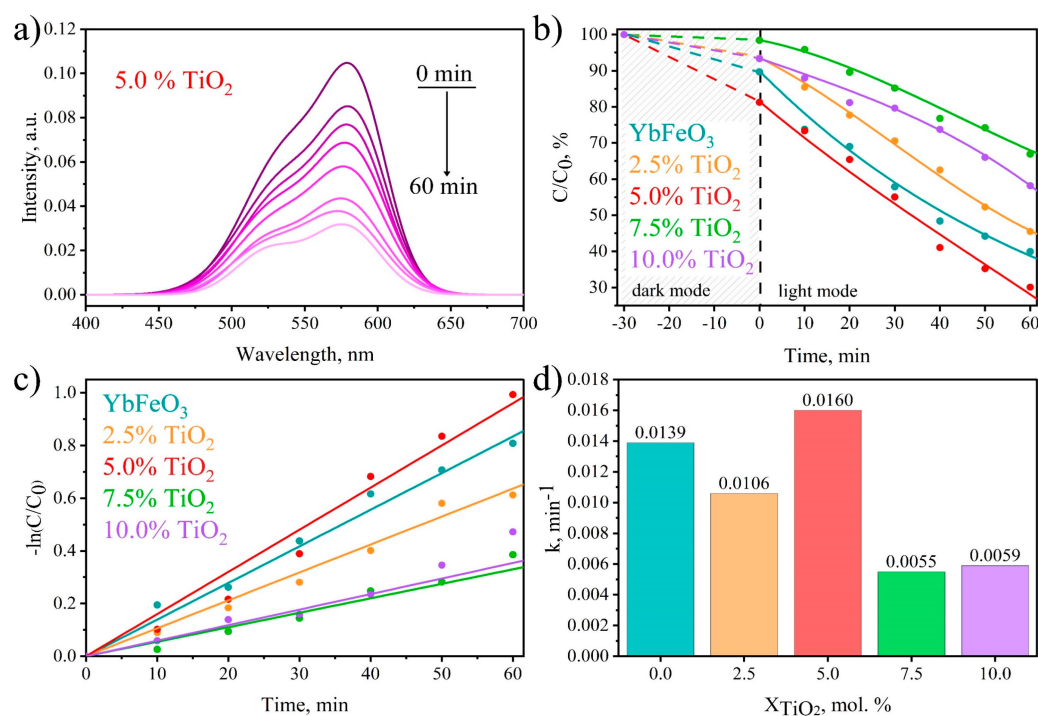

Figure 8. Photo-Fenton-like decomposition of methyl violet (MV) over h-YbFeO$_3$/o-YbFeO$_3$/TiO$_2$–5% catalyst (**a**) kinetic curves (**b**) and logarithmic kinetic curves (**c**) and photodegradation reaction rate constant (**d**) versus TiO$_2$ content.

The kinetic curves of the photodegradation of MV are presented in Figure 8b. To establish the adsorption–desorption equilibrium, the reaction solution in it was preliminarily kept in the dark for half an hour with continuous stirring. The kinetic curves showed that the degradation efficiency for each of the samples is different and depends on the mole fraction of TiO$_2$. The sample with a TiO$_2$ content of 5.0% demonstrated the highest photodecomposition efficiency, which amounted to 30.1%.

All kinetic dependences rearranged in ln(C/C$_0$) = f(t) coordinates Figure 8c are linear with good R values, which confirms the pseudo-first-order of the reaction of methyl violet photodegradation that is typical for Fenton-like processes [47]. The rate constants of the photodecomposition were established as the tangent of the slope of the linearized kinetic curves Figure 8d.

At first, the values of the rate constants increase with the addition of up to 5% of TiO$_2$ and decrease with the further addition of titanium dioxide. The initial increase is associated

with an increase in the specific surface area and the proportion of the hexagonal phase, leading to an increase in charge separation/transfer. The subsequent decrease is due to the fact that with an increase in the added TiO_2, the active centers of the photocatalyst are screened, which prevents the absorption of light, contributing to an increase in charge recombination.

Previously, it was shown that the addition of CeO_2 to the $YbFeO_3$-based nanocomposite positively affects the efficiency of photodegradation. The increase in photocatalytic activity is connected with the increment in the *h*-$YbFeO_3$ molar fraction. In previous works [28,32], the growth of the *h*-$YbFeO_3$ fraction in $YbFeO_3$ from 10.2% to 18.8% led to an increase in the photodecomposition rate constant from 0.0048 min^{-1} to 0.0138 min^{-1}. In the work, the addition of TiO_2 stabilized *h*-$YbFeO_3$, and the fraction of 41.5% was achieved, which was followed by an increase in the photodecomposition rate constant to 0.0160 min^{-1}.

3.7. Mechanism of Photo-Fenton-like Activity over o-YbFeO₃/h-YbFeO₃/TiO₂ Nanocomposites

The principally possible mechanism of photo-Fenton-like degradation of MV by heterojunction nanocomposite *h*-$YbFeO_3$/*o*-$YbFeO_3$/TiO_2 was presented in Figure 9 [37,47–49].
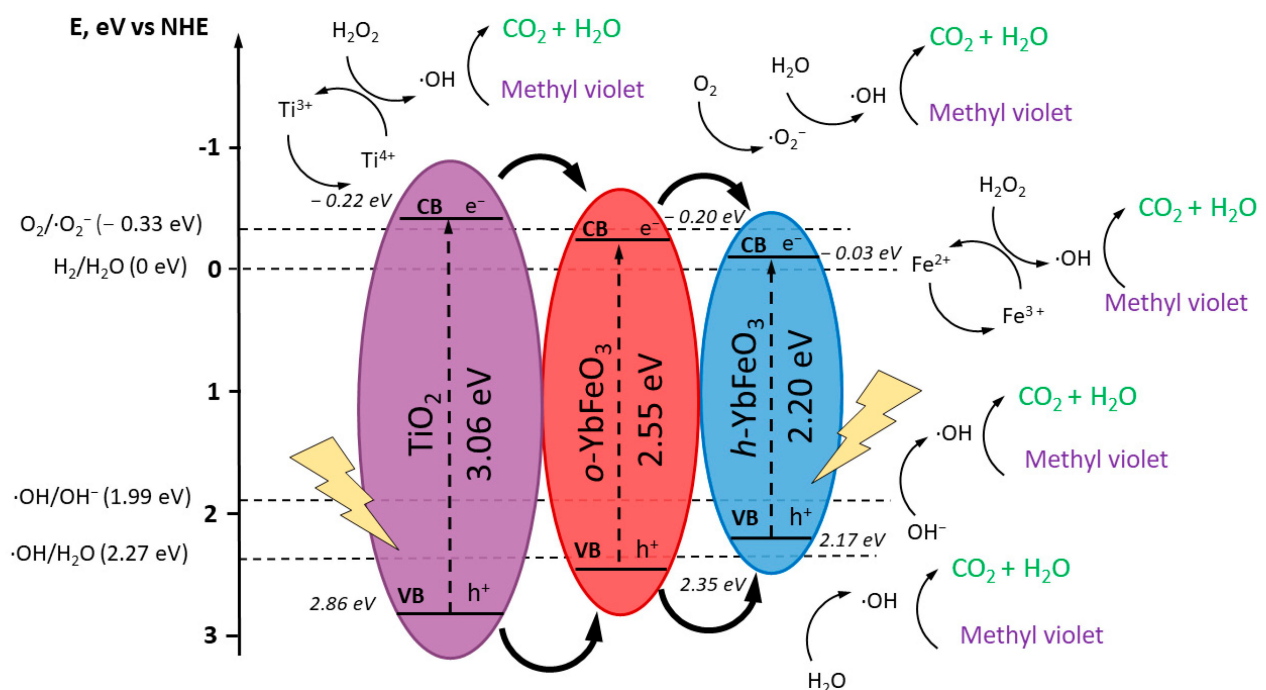

Figure 9. Schematic mechanism of photo-Fenton-like degradation of MV over *o*-$YbFeO_3$/*h*-$YbFeO_3$/TiO_2 heterojunction nanocomposite.

As the bang gap values E_g for *o*-$YbFeO_3$, *h*-$YbFeO_3$, and TiO_2 (2.55, 2.2 and 3.06 eV, respectively), correspond to absorption in the visible region, the electron–hole pairs can be formed in the components of the nanocomposite under visible light irradiation. Since the TiO_2 has the widest bang gap with the highest conduction band and the lowest valence band values among other components, the obtained nanocomposite is a combination of nested type I heterojunctions (straddling gap). Thus, the photo-generated electrons can transfer from TiO_2 to *o*-$YbFeO_3$ and then to *h*-$YbFeO_3$.

After the electron–hole pair is generated on the TiO_2 under visible light, the part of the photo-generated electrons (e$^-$) from CB TiO_2 reduces the surface cations of titanium (IV) (Ti^{4+}) to titanium (III) cations (Ti^{3+}); then hydrogen peroxide (H_2O_2) oxidizes the surface cations of titanium (III) (Ti^{3+}) to titanium (IV) (Ti^{4+}) to form hydroxyl radical (·OH) [37,48]. The reaction of ferrous ions generates highly reactive hydroxyl radicals capable of attacking and mineralizing organic pollutants. The other electrons from CB TiO_2 can migrate to CB *o*-$YbFeO_3$.

On the surface of o-YbFeO$_3$, the generation of electron–hole pairs is also available. Part of the photo-generated electrons react with oxygen (O$_2$) adsorbed on the surface of o-YbFeO$_3$ to form a superoxide anion ($\cdot$O$_{2-}$); then the superoxide anion ($\cdot$O$_2-$) reacts with water (H$_2$O) to form hydroxyl radical ($\cdot$OH). The other electrons from CB o-YbFeO$_3$ can migrate to h-YbFeO$_3$, where they take part in the same processes.

On both the o-YbFeO$_3$ and h-YbFeO$_3$ phases the photo-generated electrons (e$^-$) reduce the surface ferric cations (III) (Fe^{3+}) to ferrous cations (Fe^{2+}); then hydrogen peroxide (H$_2$O$_2$) oxidizes the surface ferrous cations (Fe^{2+}) to ferric cations (III) (Fe^{3+}) to form hydroxyl radical ($\cdot$OH).

In turn, the photo-generated holes (h^+) from VB TiO$_2$ can react with water molecules (H$_2$O) to form hydroxyl radicals ($\cdot$OH) or migrate to the VB o-YbFeO$_3$ and, finally, to h-YbFeO$_3$ to participate in the formation of hydroxyl radicals ($\cdot$OH) in the same process. Methyl violet is oxidized by $\cdot$OH to produce the two most stable products, CO$_2$ and H$_2$O.

It can be noticed that most of the generated electrons and holes migrate to the h-YbFeO$_3$ cascade. This demonstrates the leading role of the hexagonal phase in the photo-Fenton-like photodegradation of the dye.

4. Conclusions

Thus, novel I-type heterojunction nanocomposites that are based on hexagonal and orthorhombic forms of YbFeO$_3$ and titanium dioxide were successfully developed. Nanocomposites were obtained by the method of glycine–nitrate solution combustion with subsequent heat treatment of the products.

The formation features and the relative influence of the components of the nanocomposite on the formation and evolution of the polycrystalline system were studied in detail by the SEM, EDXS, and PXRD methods. The developed foamy morphology and highly porous structure cause high values of the specific surface area, contributing to an increase in the photocatalytic activity of the samples. The formation of an I-type heterojunction, confirmed by TEM and DRS data, promotes the suppression of the recombination of electron–hole pairs and positively affects the photocatalytic activity during the photo-Fenton-like photodecomposition of MV. Moreover, the addition of TiO$_2$ extra phase contributes to the stabilization of the hexagonal phase. The optimal amount of added TiO$_2$ was 5%, which is due to the high values of the specific surface area and the proportion of the hexagonal phase, as well as the processes of overlapping of the active centers of the catalyst surface by TiO$_2$ particles and an increase in charge recombination. The resulting photocatalysts based on a heterojunction nanocomposite can be used as promising photocatalysts for processes such as photo-Fenton-like oxidation of organic pollutants and other advanced oxidation techniques.

References

1. Khan, S.; Hossain, M.K. *Classification and Properties of Nanoparticles*; Elsevier Ltd.: Amsterdam, The Netherlands, 2022; ISBN 9780128242728.
2. Rahman, M.T.; Hoque, A.; Azmi, M.M.; Gafur, M.A.; Khan, R.A.; Hossain, M.K. Fe_2O_3 nanoparticles dispersed unsaturated polyester resin based nanocomposites: Effect of gamma radiation on mechanical properties. *Radiat. Eff. Defects Solids* **2019**, *174*, 480–493. [CrossRef]
3. Rahman, M.; Hoque, A.; Gafur, M.; Khan, R.A.; Hossain, M.K. Study on the mechanical, electrical and optical properties of metal-oxide nanoparticles dispersed unsaturated polyester resin nanocomposites. *Results Phys.* **2019**, *13*, 102264. [CrossRef]
4. Sławiński, W.; Przeniosło, R.; Sosnowska, I.; Suard, E. Spin reorientation and structural changes in $NdFeO_3$. *J. Phys. Condens. Matter* **2005**, *17*, 4605–4614. [CrossRef]
5. Ma, X.; Yuan, N.; Luo, X.; Chen, Y.; Kang, B.; Ren, W.; Zhang, J.; Cao, S. Field tunable spin switching in perovskite $YbFeO_3$ single crystal. *Mater. Today Commun.* **2021**, *27*, 102438. [CrossRef]
6. Downie, L.J.; Goff, R.J.; Kockelmann, W.; Forder, S.D.; Parker, J.E.; Morrison, F.D.; Lightfoot, P. Structural, magnetic and electrical properties of the hexagonal ferrites $MFeO_3$ (M=Y, Yb, In). *J. Solid State Chem.* **2012**, *190*, 52–60. [CrossRef]
7. Andrei, I. Ivanets synthesis, structure and morphology of composites based on magnesium ferrite and carbon nitride. *Dokl. Natl. Acad. Sci. Belarus* **2021**, *65*, 178–184.
8. Karpov, O.N.; Tomkovich, M.V.; Tugova, E.A. Formation of $Nd_{1-x}Bi_xFeO_3$ Nanocrystals under Conditions of Glycine-Nitrate Synthesis. *Russ. J. Gen. Chem.* **2018**, *88*, 2133–2138. [CrossRef]
9. Nguyen, A.; Nguyen, V.; Mittova, I.; Mittova, V.; Viryutina, E.; Hoang, C.C.T.; Nguyen, T.L.T.; Bui, X.; Do, T. Synthesis and magnetic properties of PrFeO3 nanopowders by the co-precipitation method using ethanol. *Nanosyst. Phys. Chem. Math.* **2020**, *11*, 468–473. [CrossRef]
10. Albadi, Y.; Sirotkin, A.A.; Semenov, V.G.; Abiev, R.S.; Popkov, V.I. Synthesis of superparamagnetic $GdFeO_3$ nanoparticles using a free impinging-jets microreactor. *Bull. Acad. Sci. USSR Div. Chem. Sci.* **2020**, *69*, 1290–1295. [CrossRef]
11. Yastrebov, S.G.; Lomanova, N.A. Specific Features in the Interaction between $BiFeO_3$ Nanoclusters Synthesized by Solution Combustion. *Tech. Phys. Lett.* **2021**, *47*, 5–8. [CrossRef]
12. Polat, O.; Coskun, M.; Coskun, F.M.; Zlamal, J.; Kurt, B.Z.; Durmus, Z.; Caglar, M.; Turut, A. Co doped $YbFeO_3$: Exploring the electrical properties via tuning the doping level. *Ionics* **2019**, *25*, 4013–4029. [CrossRef]
13. Kondrashkova, I.S.; Martinson, K.D.; Zakharova, N.V.; Popkov, V.I. Synthesis of Nanocrystalline $HoFeO_3$ Photocatalyst via Heat Treatment of Products of Glycine-Nitrate Combustion. *Russ. J. Gen. Chem.* **2018**, *88*, 2465–2471. [CrossRef]
14. Martinson, K.; Kondrashkova, I.; Omarov, S.; Sladkovskiy, D.; Kiselev, A.; Kiseleva, T.; Popkov, V. Magnetically recoverable catalyst based on porous nanocrystalline HoFeO3 for processes of n-hexane conversion. *Adv. Powder Technol.* **2019**, *31*, 402–408. [CrossRef]
15. Kostyukhin, E.M.; Kustov, A.L.; Evdokimenko, N.V.; Bazlov, A.I.; Kustov, L.M. Hydrothermal microwave-assisted synthesis of $LaFeO_3$ catalyst for N_2O decomposition. *J. Am. Ceram. Soc.* **2020**, *104*, 492–503. [CrossRef]
16. Wu, S.; Lin, Y.; Yang, C.; Du, C.; Teng, Q.; Ma, Y.; Zhang, D.; Nie, L.; Zhong, Y. Enhanced activation of peroxymonosulfte by $LaFeO_3$ perovskite supported on Al_2O_3 for degradation of organic pollutants. *Chemosphere* **2019**, *237*, 124478. [CrossRef]
17. Li, L.; Wang, X.; Zhang, Y. Enhanced visible light-responsive photocatalytic activity of LnFeO3 (Ln=La, Sm) nanoparticles by synergistic catalysis. *Mater. Res. Bull.* **2014**, *50*, 18–22. [CrossRef]
18. Ivanets, A.I. Catalytic Degradation of Methylene Blue on Magnesium Ferrite Doped with Lanthanides. *J. Water Chem. Technol.* **2021**, *43*, 193–199. [CrossRef]
19. Shifrina, Z.B.; Bronstein, L.M. Magnetically Recoverable Catalysts: Beyond Magnetic Separation. *Front. Chem.* **2018**, *6*, 298. [CrossRef]
20. Albadi, Y.; Martinson, K.; Shvidchenko, A.; Buryanenko, I.; Semenov, V.; Popkov, V. Synthesis of $GdFeO_3$ nanoparticles via low-temperature reverse co-precipitation: The effect of strong agglomeration on the magnetic behavior. *Nanosyst. Phys. Chem. Math.* **2020**, *11*, 252–259. [CrossRef]
21. Jurgons, R.; Seliger, C.; Hilpert, A.; Trahms, L.; Odenbach, S.; Alexiou, C. Drug loaded magnetic nanoparticles for cancer therapy. *J. Phys. Condens. Matter* **2006**, *18*, S2893–S2902. [CrossRef]
22. Darwish, M.S.A.; Kim, H.; Lee, H.; Ryu, C.; Yoon, J. Synthesis of Magnetic Ferrite Nanoparticles with High Hyperthermia Performance via a Controlled Co-Precipitation Method. *Nanomaterials* **2019**, *9*, 1176. [CrossRef] [PubMed]
23. De Jong, W.H.; Borm, P.J.A. Drug delivery and nanoparticles: Applications and hazards. *Int. J. Nanomed.* **2008**, *3*, 133–149. [CrossRef] [PubMed]
24. Zhang, P.; Qin, H.; Lv, W.; Zhang, H.; Hu, J. Gas sensors based on ytterbium ferrites nanocrystalline powders for detecting acetone with low concentrations. *Sens. Actuators B Chem.* **2017**, *246*, 9–19. [CrossRef]
25. Zhang, P.; Qin, H.; Zhang, H.; Lü, W.; Hu, J. CO_2 gas sensors based on $Yb_{1-x}Ca_xFeO_3$ nanocrystalline powders. *J. Rare Earths* **2017**, *35*, 602–609. [CrossRef]
26. Fortuño-Morte, M.; Serna-Gallén, P.; Beltrán-Mir, H.; Cordoncillo, E. A new series of environment-friendly reddish inorganic pigments based on AFeO3 (A = Ln, Y) with high NIR solar reflectance. *J. Mater.* **2021**, *7*, 1061–1073. [CrossRef]

27. Solomonov, A.V.; Marfin, Y.; Rumyantsev, E.V. Design and applications of dipyrrin-based fluorescent dyes and related organic luminophores: From individual compounds to supramolecular self-assembled systems. *Dye. Pigment.* **2019**, *162*, 517–542. [CrossRef]

28. Tikhanova, S.M.; Lebedev, L.A.; Martinson, K.D.; Chebanenko, M.I.; Buryanenko, I.V.; Semenov, V.G.; Nevedomskiy, V.N.; Popkov, V.I. The synthesis of novel heterojunction h-YbFeO$_3$/o-YbFeO$_3$ photocatalyst with enhanced Fenton-like activity under visible-light. *New J. Chem.* **2021**, *45*, 1541–1550. [CrossRef]

29. Li, C.; Soh, K.C.K.; Wu, P. Formability of ABO$_3$ perovskites. *J. Alloy. Compd.* **2004**, *372*, 40–48. [CrossRef]

30. Kumar, M.S.V.; Kuribayashi, K.; Kitazono, K. Effect of Oxygen Partial Pressure on the Formation of Metastable Phases from an Undercooled YbFeO$_3$Melt Using an Aerodynamic Levitator. *J. Am. Ceram. Soc.* **2009**, *92*, 903–910. [CrossRef]

31. Hosokawa, S.; Jeon, H.-J.; Inoue, M. Thermal stabilities of hexagonal and orthorhombic YbFeO$_3$ synthesized by solvothermal method and their catalytic activities for methane combustion. *Res. Chem. Intermed.* **2011**, *37*, 291–296. [CrossRef]

32. Tikhanova, S.M.; Lebedev, L.A.; Kirillova, S.A.; Tomkovich, M.V.; Popkov, V.I. Synthesis, structure, and visible-light-driven activity of o-YbFeO$_3$/h-YbFeO$_3$/CeO$_2$ photocatalysts. *Chim. Techno Acta* **2021**, *8*, 20218407. [CrossRef]

33. Popkov, V.; Almjasheva, O.; Nevedomskiy, V.; Sokolov, V.; Gusarov, V. Crystallization behavior and morphological features of YFeO$_3$ nanocrystallites obtained by glycine-nitrate combustion. *Nanosyst. Phys. Chem. Math.* **2015**, *6*, 866–874. [CrossRef]

34. Ivanets, A.I.; Srivastava, V.; Roshchina, M.Y.; Sillanpää, M.; Prozorovich, V.G.; Pankov, V.V. Magnesium ferrite nanoparticles as a magnetic sorbent for the removal of Mn^{2+}, Co^{2+}, Ni^{2+} and Cu^{2+} from aqueous solution. *Ceram. Int.* **2018**, *44*, 9097–9104. [CrossRef]

35. Voskanyan, A.A.; Chan, K.-Y.; Li, C.-Y.V. Colloidal Solution Combustion Synthesis: Toward Mass Production of a Crystalline Uniform Mesoporous CeO$_2$ Catalyst with Tunable Porosity. *Chem. Mater.* **2016**, *28*, 2768–2775. [CrossRef]

36. Deganello, F.; Testa, M.L.; La Parola, V.; Longo, A.; Tavares, A.C. LaFeO$_3$-based nanopowders prepared by a soft–hard templating approach: The effect of silica texture. *J. Mater. Chem. A* **2014**, *2*, 8438–8447. [CrossRef]

37. Seroglazova, A.S.; Chebanenko, M.I.; Popkov, V.I. Synthesis, structure, and photo-Fenton activity of PrFeO$_3$-TiO$_2$ mesoporous nanocomposites. *Kondens. Condens. Matter Interphases* **2021**, *23*, 548–560. [CrossRef]

38. Tao, Y.-G.; Xu, Y.-Q.; Pan, J.; Gu, H.; Qin, C.-Y.; Zhou, P. Glycine assisted synthesis of flower-like TiO$_2$ hierarchical spheres and its application in photocatalysis. *Mater. Sci. Eng. B* **2012**, *177*, 1664–1671. [CrossRef]

39. Eswar, N.K.; Ramamurthy, P.C.; Madras, G. High photoconductive combustion synthesized TiO$_2$derived nanobelts for photocatalytic water purification under solar irradiation. *New J. Chem.* **2015**, *39*, 6040–6051. [CrossRef]

40. Sklyarova, A.; Popkov, V.I.; Pleshakov, I.V.; Matveev, V.V.; Štěpánková, H.; Chlan, V. Peculiarities of 57 Fe NMR Spectrum in Micro- and Nanocrystalline Europium Orthoferrites. *Appl. Magn. Reson.* **2020**, *51*, 1701–1710. [CrossRef]

41. Martinson, K.; Ivanov, V.; Chebanenko, M.; Panchuk, V.; Semenov, V.; Popkov, V. Facile combustion synthesis of TbFeO3 nanocrystals with hexagonal and orthorhombic structure. *Nanosyst. Phys. Chem. Math.* **2019**, *10*, 694–700. [CrossRef]

42. Popkov, V.I.; Martinson, K.D.; Kondrashkova, I.S.; Enikeeva, M.O.; Nevedomskiy, V.N.; Panchuk, V.V.; Semenov, V.G.; Volkov, M.P.; Pleshakov, I.V. SCS-assisted production of EuFeO3 core-shell nanoparticles: Formation process, structural features and magnetic behavior. *J. Alloys Compd.* **2021**, *859*, 157812. [CrossRef]

43. Rai, R.C.; Horvatits, C.; Mckenna, D.; Du Hart, J. Structural studies and physical properties of hexagonal-YbFeO$_3$ thin films. *AIP Adv.* **2019**, *9*, 015019. [CrossRef]

44. Huang, Y.; Wei, Y.; Wang, J.; Luo, D.; Fan, L.; Wu, J. Controllable fabrication of Bi2O$_3$/TiO$_2$ heterojunction with excellent visible-light responsive photocatalytic performance. *Appl. Surf. Sci.* **2017**, *423*, 119–130. [CrossRef]

45. Zhang, D.; Dong, S. Challenges in band alignment between semiconducting materials: A case of rutile and anatase TiO$_2$. *Prog. Nat. Sci.* **2019**, *29*, 277–284. [CrossRef]

46. Fan, X.; Hao, H.; Shen, X.; Chen, F.; Zhang, J. Removal and degradation pathway study of sulfasalazine with Fenton-like reaction. *J. Hazard. Mater.* **2011**, *190*, 493–500. [CrossRef]

47. Makhotkina, O.; Preis, S.; Parkhomchuk, E. Water delignification by advanced oxidation processes: Homogeneous and heterogeneous Fenton and H$_2$O$_2$ photo-assisted reactions. *Appl. Catal. B Environ.* **2008**, *84*, 821–826. [CrossRef]

48. Punjabi, P.B. *Fenton and Photo-Fenton Processes*; Udaipur: Rajasthan, India, 2018; ISBN 9780128104996.

49. Liu, J.; He, F.; Chen, L.; Qin, X.; Zhao, N.; Huang, Y.; Peng, Y. Novel hexagonal-YFeO$_3$/α-Fe$_2$O$_3$ heterojunction composite nanowires with enhanced visible light photocatalytic activity. *Mater. Lett.* **2016**, *165*, 263–266. [CrossRef]